Potassium tune-out-wavelength measurement using atom interferometry and a multipass optical cavity

Raisa Trubko,[1] Maxwell D. Gregoire,[2] William F. Holmgren,[2] and Alexander D. Cronin[1,2]
[1]*College of Optical Sciences, University of Arizona, Tucson, Arizona 85721, USA*
[2]*Department of Physics, University of Arizona, Tucson, Arizona 85721, USA*
(Received 12 April 2017; published 26 May 2017)

The longest tune-out wavelength for potassium atoms, $\lambda_{zero} = 768.9701(4)$ nm, was measured using an atom interferometer with a large irradiance gradient supported in a multipass optical cavity. Systematic errors in λ_{zero} measurements that arise from laser light, Doppler shifts, and the Earth's rotation are described. The ratio of oscillator strengths for the potassium $D2$ and $D1$ lines inferred from this λ_{zero} measurement is $\rho = f_{D2}/f_{D1} = 2.0066(11)$, and the ratio of line strengths is $R = S_{D2}/S_{D1} = 1.9977(11)$.

DOI: 10.1103/PhysRevA.95.052507

Tune-out wavelengths (λ_{zero}) are associated with roots in the dynamic polarizability spectrum of an atom. Light at a tune-out wavelength therefore causes zero energy shift (no ac Stark shift) for atoms in a particular state. Precise λ_{zero} measurements [1–5] serve as a means to study several atomic properties including lifetimes; oscillator strengths; oscillator strength ratios; atomic scalar, vector, and tensor polarizabilities and hyperpolarizabilities; the polarization of atomic core electrons; core-valence electron correlations; and relativistic and QED effects on atomic transition amplitudes [6–15]. Improved knowledge of λ_{zero} values can also be important for several experiments that use species-specific and state-specific optical dipole potentials created with light near a tune-out wavelength [16–23]. Tune-out wavelengths, also known as magic-zero wavelengths, were mentioned in 2004 by Safronova *et al.* [6]. They were introduced in more detail in 2007 by LeBlanc and Thywissen [16], and more precise calculations of several λ_{zero} were presented in 2011 by Arora *et al.* [7]. The most accurate measurements of tune-out wavelengths to date have used atom diffraction [1,5], atom interferometry [2,3], and studies of trapped atom dynamics [4].

Here we present an improved measurement of the longest tune-out wavelength for potassium, $\lambda_{zero} = (786\,970.14 \pm 0.41)$ pm. We describe how we made this measurement using a multipass optical cavity to recycle light shining on an atom interferometer. Then we discuss methods we used to reduce errors and estimate systematic uncertainties. We interpret this measurement in terms of the ratio of line strengths,

$$R = \frac{S_{D2}}{S_{D1}} = \frac{|\langle 4s\|D\|4p_{3/2}\rangle|^2}{|\langle 4s\|D\|4p_{1/2}\rangle|^2} = 1.9977(11), \tag{1}$$

and the ratio of oscillator strengths,

$$\rho = \frac{f_{D2}}{f_{D1}} = R\left(\frac{\omega_{D2}}{\omega_{D1}}\right) = 2.0066(11), \tag{2}$$

for the $D1$ and $D2$ lines in potassium associated with the $4s$-$4p_{1/2}$ and $4s$-$4p_{3/2}$ transitions. We discuss the impact of this measurement on our knowledge of the $4p_{1/2}$ and $4p_{3/2}$ state lifetimes.

To measure λ_{zero} we applied an irradiance gradient on the paths of a three-nanograting Mach-Zehnder atom beam interferometer [24–26] as shown in Fig. 1. Then we report the root in the light-induced phase-shift spectrum,

$$\phi(\omega) = \frac{\alpha(\omega)}{2c\hbar\epsilon_o v}\int s\frac{d}{dx}I(x,y;\omega)\,dy, \tag{3}$$

where $\omega = 2\pi c/\lambda$ is the laser frequency, v is the atom beam velocity, s is the atom wave-packet separation, and dI/dx is the irradiance gradient. Figure 1 shows the coordinate axes.

I. MULTIPASS CAVITY ENHANCEMENT

To improve the precision of λ_{zero} measurements we built an optical cavity that increases the line integral of the irradiance gradient $\int \frac{dI}{dx}dy$. We used an optical fiber to guide light directly into the vacuum chamber and to launch a laser beam into a multipass optical cavity (MPC). The MPC is made of two plane mirrors separated by $\ell = 1$ cm. The mirrors surround the atom beam as sketched in Fig. 1 so atoms interact with approximately 40 passes of the laser beam. This is not a stable resonator (the laser spots walk and grow without bound), so we refer to it as a multipass cavity (MPC).

To quantify the benefit of the MPC we first discuss the phase shift ϕ_{single} caused by a single laser beam propagating in $\hat{z}$ with an irradiance profile $I = [2P/(\pi w^2)]\exp[-2(x^2+y^2)/w^2]$, where P is the power and w is the beam width (radius at e^{-2} irradiance). From Eq. (3), the phase $\phi_{single} \propto \int \frac{dI}{dx}dy = [8Px/(\sqrt{2\pi}w^3)]\exp[-2x^2/w^2]$ is maximized when the laser beam center is offset from the atom beam paths by $x = w/2$. Then, with that optimized alignment, $\phi_{single} \propto |\int \frac{dI}{dx}dy|_{max} = (8/e\pi)^{-1/2}(P/w^2)$. Because the laser beam width is large compared to the $s = 20\,\mu$m separation of the atom interferometer paths ($w \gg s$), we neglect higher-order derivatives, e.g., $\frac{d^2}{dx^2}\int I\,dy$. We find the maximum phase shift due to a single pass of a laser beam is

$$\phi_{single} = \left(\frac{2}{e\pi}\right)^{-1/2}\frac{\alpha(\omega)s}{c\hbar\epsilon_o v}\frac{P}{w^2}. \tag{4}$$

Since ϕ_{single} is proportional to P/w^2, we are motivated to use a smaller waist to get a bigger signal. However, the 60-μm thickness of the atom beam sets a constraint on the minimum waist w. If the laser beam is smaller than this, it tends to reduce the ensemble- averaged light-induced phase shift and contrast. Therefore, we chose $w \approx 60\ \mu$m to produce a more uniform irradiance gradient across all of the atom beam paths.

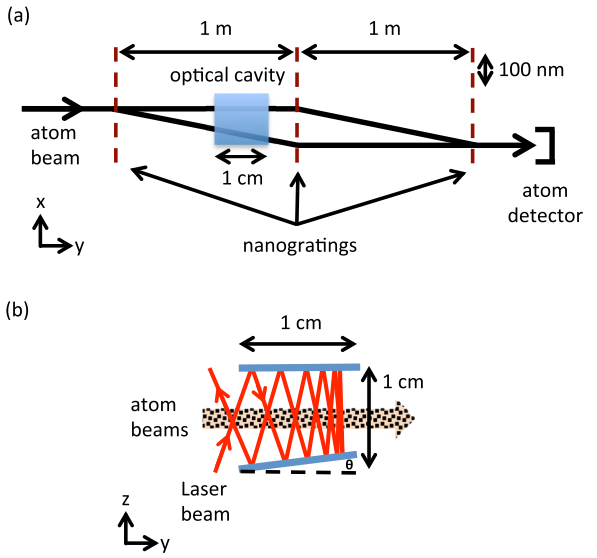

FIG. 1. (a) Top-view schematic of atom interferometer paths passing through a multipass optical optical cavity. (b) Side-view schematic of the plane-plane optical multipass cavity aligned so atoms interact with multiple passes of the laser beam. The deviation from parallel is exaggerated to show how the laser beam folds back at different angles.

Fully separated interferometer paths would enable us to apply light on one path while leaving the other path through the interferometer completely in the dark, as demonstrated in [3]. This would cause a phase $\phi_1 = \alpha(\omega)/(2c\hbar\epsilon_o v)\int I(\omega)\,dy$ that is larger than the gradient-induced phase shift in Eq. (4) by the ratio $\phi_1/\phi_{\text{single}} = (\sqrt{e}/2)(w/s)$. However, producing such well-separated atom beam paths requires improved collimation and/or larger diffraction angles, both of which reduce the atomic flux in our apparatus. An alternative method to increase ϕ without reducing atomic flux is to use more laser power or recycle the laser light.

That is why we constructed a MPC to recycle light and thus increase light-induced phase shifts. Because the MPC sketched in Fig. 1(b) is built with two plane mirrors, the laser beam diameter eventually grows as the laser propagates in the MPC. Therefore, one might expect that there is a tradeoff between a small waist or a long Raleigh range, but this is not the case. Even though a smaller waist causes a larger signal for a single pass of the laser beam, a long Raleigh range makes several passes contribute significantly to ϕ. These factors compensate as shown with Eqs. (5) and (6).

The MPC enhances the signal by the factor

$$\frac{\phi_{\text{multi}}}{\phi_{\text{single}}} = w_0^2 \sum_n \frac{R'^n}{[w'(z')]^2}, \tag{5}$$

where R' is the reflectivity of the mirrors and $w'(z') = w_0'[1 + (z'/z_{\text{R}}')^2]^{1/2}$ is the laser beam width. $z' = n\ell$ after n reflections in the plane-plane cavity where ℓ is the separation between the two mirrors, and $n = 0$ corresponds to the laser beam waist location. The Raleigh range is $z_{\text{R}}' = \pi w_0'^2/\lambda$. We use primes ($w'$, z', and R') to indicate quantities for the laser beam in the MPC.

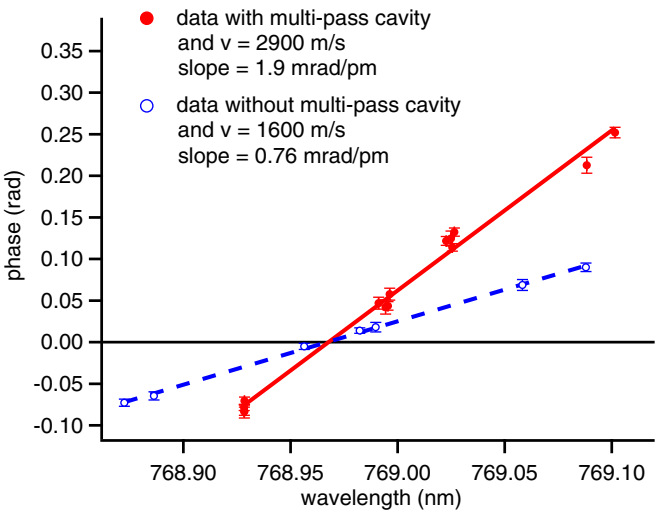

FIG. 2. Enhanced slope for phase vs wavelength data due to multipass cavity. The slope for ϕ_{multi} is $d\phi/d\lambda = 1.9$ mrad/pm with $v = 2900$ m/s atoms (solid line and solid circles). A smaller slope of 0.76 mrad/pm was observed for a single-pass experiment (ϕ_{single}) with $v = 1600$ m/s atoms (dashed line and open circles).

For comparison, w_0 is the waist in a single-pass experiment. For high-reflectivity mirrors ($R \approx 1$) and $z_{\text{R}}' \gg \ell$, we approximate the sum in Eq. (5) with the integral $\int [w'(z')]^{-2}\,dz'/\ell$ to find the enhancement factor:

$$\frac{\phi_{\text{multi}}}{\phi_{\text{single}}} = \pi\left(\frac{w_0}{w_0'}\right)^2\left(\frac{z_{\text{R}}'}{\ell}\right) = \pi^2\frac{w_0^2}{\lambda\ell}. \tag{6}$$

The last form shows that the enhancement is independent of w_0' and z_{R}'. For our experiments with $w_0 = 60$ μm, $\lambda = 769$ nm, and $\ell = 1.0$ cm, Eq. (6) yields a calculated enhancement of $\aleph = 4.6$. With reflectivity $R' = 99.7\%$, Eq. (5) predicts $\aleph = 4.0$.

We experimentally verified that our MPC increased the signal slope as shown in Fig. 2. With the MPC, the slope of $d\phi/d\lambda = 1.9$ mrad/pm with 2900 m/s potassium atoms was significantly larger than the slope $d\phi/d\lambda = 0.76$ mrad/pm that we observed with a single pass of the laser beam. This was true even though we had used slower (1600 m/s) potassium atoms for the single-pass experiments. For a more direct comparison, because the signal slope depends on v^{-2} we predict that a single-pass experiment with 2900 m/s potassium atoms in our experiment would have an even smaller slope of 0.23 mrad/pm. This predicted single-pass slope is 8.2 times smaller than the slope we observed with the MPC. This validates that the MPC is serving its purpose. The data with the MPC used for the tune-out wavelength measurement presented here were obtained over 9 days with an average signal slope of 2.1 mrad/pm and an rms distribution of 0.5 mrad/pm.

Our experiment also benefited from improved mechanical stability associated with the MPC and with bringing the laser into the atom interferometer vacuum chamber via an optical fiber. Repeated measurements of λ_{zero} demonstrated less scatter than we had in [2] by factor of 6. The MPC improved our statistical precision for λ_{zero} measurements from 1.4 pm in [2] to 0.3 pm in the present work. In each case we quote a 2σ statistical uncertainty (where σ is the standard

error of the mean [27]), and both [2] and this measurement used approximately 30 h of data.

Another example of an optical cavity to enhance irradiance on an atom interferometer was described by Hamilton *et al.* [28], who used intracavity light to make an atom interferometer. In comparison, we only used a cavity as an interaction region. Yet, similar to Hamilton *et al.*, we benefit from increased light-atom interactions intracavity. In principle, a resonant cavity with curved mirrors can further increase irradiance and maintain smaller beam waists in a cavity mode, both factors which would increase $d\phi/d\lambda$. Resonant cavities can also serve as a spectral filter, which can be both beneficial and detrimental as we discuss in the section on tuning out broadband light (Sec. IV).

II. CHOICE OF ATOM VELOCITY

Experimentally, we found it more favorable to work with velocities of 2900 m/s as compared to 1600 m/s. So, here we discuss reasons why there may be an optimum atom beam velocity for λ_{zero} measurements with our apparatus. The velocity of the atoms has an effect on the signal-to-noise ratio for two reasons. First, slower atoms receive larger light-induced phase shifts because the signal ϕ is proportional to v^{-2}. This is because the interaction time is proportional to $1/v$, and the separation, s in Eq. (3), depends on the de Broglie wavelength $\lambda_{\text{dB}} = h/mv$. However, slower atom beams also have much lower atom count rates ($N \propto v^3$) and therefore worse statistical precision (shot noise) in phase described by $\delta\phi = (C\sqrt{N})^{-1}$. Thus, the shot noise limited signal-to-noise ratio is

$$R_{\text{S/N}} = \frac{\phi}{\delta\phi} \propto \frac{C}{\sqrt{v}} \tag{7}$$

This naïve estimate shows that higher signal-to-noise ratios would be obtained with velocity as low as possible. However, this assumed zero detector background noise and zero drifts in the laser wavelength, laser power, laser beam alignment, and atom fringe reference phase over time.

If we consider a more realistic model with a flux-independent background (average) atom count rate due to detector noise, then we find there is an optimum atom beam velocity. If the observed counts $N = N_0 + B$ are the sum of N_0 detected atoms and B background counts, this increases the fluctuations in counts and reduces contrast so

$$C = C_0 \frac{N_0}{N_0 + B}, \tag{8}$$

where C_0 is the contrast that would be observed if $B = 0$. Then

$$\delta\phi = \frac{1}{C\sqrt{N}} = \frac{\sqrt{N_0 + B}}{C_0 N_0} \tag{9}$$

and

$$R_{\text{S/N}} = \frac{\phi}{\delta\phi} \propto \frac{v^{-2} C_0 N_0}{\sqrt{N_0 + B}}. \tag{10}$$

Now let $N_0 = kv^3$, where $k = 100B/(3\ \text{km/s})^3$ is typical. This means that the background B is about 1% of the count rate that we observe with 3 km/s atom beams. Then we find the velocity that maximizes $R_{\text{S/N}}$ is

$$v = \left(\frac{2B}{k}\right)^{1/3} = 814\ \text{m/s}. \tag{11}$$

This model of signal to noise identifies a nonzero optimum velocity. Additional phase noise due to drifts in alignment will make the optimum velocity even higher. This is because faster atoms provide higher flux, and this enables us to operate experiments faster and thus control for drifts better. Hence, our selection of 2–3 km/s atoms may be close to optimal.

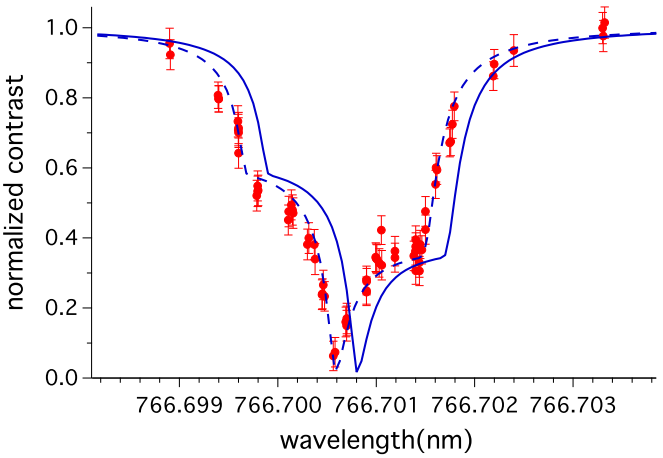

FIG. 3. Decoherence spectroscopy data (solid red circles) showing contrast vs laser wavelength. Theoretical curves are shown in solid blue for no Doppler shift and dashed blue for a −0.21-pm Doppler shift. The best-fit model indicates that a +0.21-pm shift should be added to our λ_{zero} measurements due to Doppler shifts in the MPC [29].

III. DECOHERENCE SPECTROSCOPY

The MPC causes a set of Doppler shifts. As indicated in Fig. 1 we do not have a simple crossed-beam experiment. Instead there are many laser beams crossing at different angles relative to the atom beam.

To measure the range of Doppler shifts in our multipass cavity we developed *decoherence spectroscopy* [29]. This technique uses quantum decoherence due to photon scattering to cause laser-wavelength-dependent contrast loss.

For decoherence spectroscopy we used the same experimental laser beam and atom beam geometry as we did for λ_{zero} measurements, but the laser wavelength is tuned near resonance (across the $D2$ line). The laser power is also attenuated by several orders of magnitude to reduce power broadening. Then, we monitor the atom interference fringe contrast as a function of laser wavelength as shown in Fig. 3.

A model decoherence spectrum shown as a dotted blue line in Fig. 3 makes the best fit to the decoherence data. The theory used for the fits to the data is explained in [29]. The measured contrast spectrum is shifted by (-0.21 ± 0.10) pm from the theoretical prediction. Therefore, we apply a $(+0.21 \pm 0.10)$ pm correction to our λ_{zero} measurement. This correction accounts for the net Doppler shift in our experiment and for any systematic errors of the Bristol 621B wavemeter that we use to measure the laser wavelength.

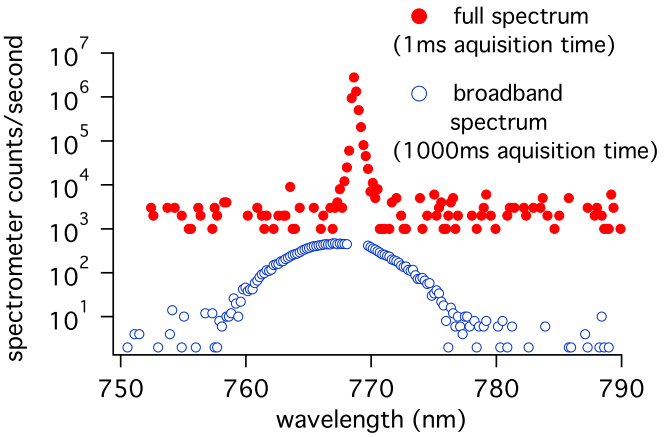

FIG. 4. Power spectrum output from our tapered amplifier. The broadband spectrum (open blue circles) was observed with 1000 times more acquisition time while using a dark fringe from an etalon to suppress the monochromatic component of the spectrum, as described in this paper. A spectrum with the monochromatic light tuned to a bright fringe of the etalon is shown with solid red circles.

IV. TUNING OUT BROADBAND LIGHT

Broadband light from a tapered amplifier (TA) laser can cause errors in λ_{zero} measurements. Therefore, we measured the spectrum of broadband emission of our TA and controlled it in order to minimize systematic errors in λ_{zero}.

For more background, as discussed by Bolpasi and von Klitzing [30], there are several categories of atomic physics experiments for which broadband light causes problems such as heating, decoherence, or background signals. There are also some types of experiments such as fluorescence spectroscopy and magneto-optical trapping that are not adversely affected by a small amount of off-mode light. However, in experiments to measure λ_{zero}, broadband light near a resonance can add significant light-induced phase shifts.

To minimize broadband light we saturate the TA [31] with 20 mW of light from an external cavity diode laser [32] after an optical isolator, and spatially filter the 1.2-W TA output by focusing it into a single-mode optical fiber [33] after another optical isolator. The fiber brings 200 mW of light into the multipass cavity in vacuum.

To measure the broadband spectrum shown in Fig. 4, we used a grating spectrometer [34] in conjunction with a thin (1-mm) glass etalon, which increases the effective dynamic range of the spectrometer. A dark fringe and bright fringe are used alternately to suppress or transmit the monochromatic component of the laser. A dark fringe in reflection from the etalon suppresses the monochromatic component of the laser by a factor of 1000, whereas the broadband light spectrum is spread over many etalon fringes. Etalon fringes are not resolved in Fig. 4 since the 0.2-nm (100-GHz) free spectral range of the etalon is five times smaller than the 1-nm resolution of the grating spectrometer. Thus, the power of the broadband light spectrum is two times larger than what is measured and we make a correction for this effect. Suppressing the monochromatic light increased the dynamic range of our spectrometer system sufficiently for us to measure the broadband spectrum when the TA was seeded. For comparison, the unseeded TA light has about three times more power and a 1–2-nm bluer broadband spectrum (not shown). We observed the broadband spectrum shown in Fig. 4 using a 1-s acquisition time. We measured the relative power in the monochromatic peak using a maximum in reflection from the etalon (a bright fringe) and reducing the spectrometer acquisition time to 1 ms. The asymmetric spectral peak reported for the monochromatic light in Fig. 4 is due to the spectrometer's response, as we verified using a monochromatic HeNe laser.

Scanning the seed laser wavelength by 1 nm causes no observed changes in the broadband spectrum of the laser. This is important because to measure $\phi(\lambda)$ we scan the wavelength of the seed laser on either side of λ_{zero} as shown in Fig. 2. Also of note, the peak wavelength of the broadband spectral component depends on the temperature of the TA's water-cooled mount. With this, we can minimize shifts in $\phi(\lambda)$ caused by broadband light by adjusting the TA temperature.

To model how broadband light affects our λ_{zero} measurement, we write the TA output spectrum as a monochromatic component plus a broadband component:

$$P_{laser}(\lambda) = P_{mono}(\lambda) + P_{broad}(\lambda). \tag{12}$$

A delta-function spectrum describes the amplified monochromatic laser light, $P_{mono}(\lambda) = P_M\delta(\lambda - \lambda_M)$, where P_M is the power of the monochromatic component and λ_M is the wavelength of the monochromatic component. A Gaussian distribution describes the broadband component, $P_{broad}(\lambda) = P_{BB}(\sigma_{BB}\sqrt{2\pi})^{-1}\exp[-(\lambda-\lambda_{BB})^2/(2\sigma_{BB}^2)]$, where P_{BB} is the power of the broadband component, λ_{BB} is the peak wavelength of the broadband distribution, and σ_{BB} is the rms width of the Gaussian broadband distribution. This representation leads to a two-component model of the phase shift

$$\phi_{total}(\lambda_M) = \phi(\lambda_M) + \phi_{BB}, \tag{13}$$

where $\phi(\lambda_M)$ is given by Eq. (3) with $\omega = 2\pi c/\lambda_M$, and the phase shift due to the broadband radiation from the seeded TA is

$$\phi_{BB} = \frac{1}{2\epsilon_o c\hbar v}\int\int s\,\alpha(\omega)\frac{dI_{broad}(\omega;x,y)}{dx}\,dy\,d\omega \tag{14}$$

with the spectrum of $I_{broad}(\omega;x,y)$ found from the measured $P_{broad}(\lambda)$. Then the shift in measured λ_{zero} caused by ϕ_{BB} is

$$\delta\lambda_{zero} = \phi_{BB}\left(\frac{d\phi}{d\lambda}\right)^{-1}. \tag{15}$$

As shown in Fig. 5, the shift $\delta\lambda_{zero}$ is an antisymmetric function of λ_{BB}. Therefore, we can tune the broadband spectrum to make $\delta\lambda_{zero} = 0$.

If the spectral width of the broadband radiation is larger than the fine structure splitting, $\sigma_{BB} > \Delta\lambda_{FS}$, then a peak wavelength λ_{BB} near

$$\lambda_{BB,zero} \approx \lambda_{D2} + \frac{f_{D1}}{f_{D1}+f_{D2}}\Delta\lambda_{FS} \tag{16}$$

can null ϕ_{BB} and thus minimize error in λ_{zero}. This $\lambda_{BB,zero}$ is the peak wavelength for a broadband spectral component that causes zero phase shift. So we call $\lambda_{BB,zero}$ the *broadband tune-out wavelength*. Here, the fine structure splitting is denoted by $\Delta\lambda_{FS} \equiv \lambda_{D1} - \lambda_{D2}$, and for K, $\Delta\lambda_{FS} = 3.4$ nm. To derive Eq. (16) we express dynamic polarizability as a

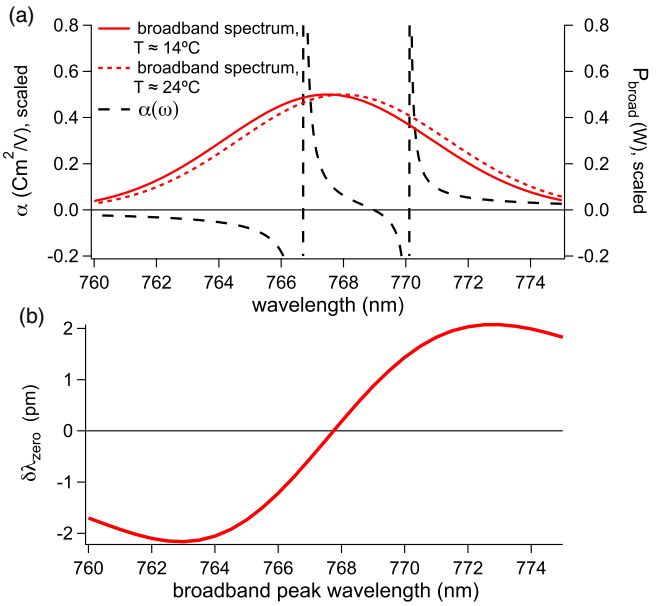

FIG. 5. Error in λ_{zero} due to broadband light. (a) Spectra of $\alpha(\omega)$ and P_{broad} vs wavelength used in Eq. (14) to calculate ϕ_{BB}. Two different P_{broad} spectra indicate how temperature-tuning the tapered amplifier laser adjusts the peak wavelength λ_{BB} of the broadband light. P_{broad} and $\alpha(\omega)$ are scaled in order to be viewed conveniently on the same graph. (b) Resulting error ($\delta\lambda_{\text{zero}}$) as a function of the broadband peak wavelength λ_{BB}.

sum over states with just the $D1$ and $D2$ excitations, we ignore α_r in Eq. (17), and we make the near-resonance approximation that $\omega_{D1}^2 - \omega^2 \approx 2\omega(\omega_{D1} - \omega)$. Hence $\lambda_{\text{BB,zero}}$ is approximate, but it is significantly different than λ_{zero}. For alkali-metal atoms with an oscillator strength ratio [see Eq. (2)] of $\rho \approx 2$ we find the broadband tune-out wavelength is approximately $\lambda_{\text{BB,zero}} = \lambda_{D2} + (1/3)\Delta\lambda_{\text{FS}}$, whereas the tune-out wavelength for monochromatic light is approximately $\lambda_{\text{zero}} = \lambda_{D2} + (2/3)\Delta\lambda_{\text{FS}}$. For narrower broadband spectra (so the inequality $\sigma_{\text{BB}} > \lambda_{\text{FS}}$ is no longer satisfied) the peak wavelength that minimizes ϕ_{BB} will shift from $\lambda_{\text{BB,zero}}$ towards λ_{zero}.

We controlled λ_{BBpeak} by adjusting the temperature of the tapered amplifier mount (to 14 °C) with the goal of making $\lambda_{\text{BB}} = \lambda_{\text{BB,zero}}$. We used the spectrometer and etalon system to measure $\lambda_{\text{BB}} = 767.5(3)$ nm, and $\sigma_{\text{BB}} = 5(1)$ nm, and $P_{\text{M}}/P_{\text{BB}} = 370(40)$. With these data we used Eqs. (14) and (15) to infer that broadband light caused a systematic error of $-0.08(8)$ pm for our tune-out-wavelength measurement. Therefore, we applied a correction of $+0.08(8)$ pm before we presented our final result for λ_{zero}. This correction and the uncertainty in this correction are smaller than the statistical precision of our λ_{zero} measurement.

V. MINIMIZING ERRORS DUE TO EARTH'S ROTATION

In [22], we reported large (± 200 pm) systematic shifts in measured tune-out wavelengths, $\lambda_{\text{zero,lab}}$, due to the Earth's rotation rate, Ω_E, and elliptically polarized light. Such errors stem from balancing the Coriolis force with atomic-spin-dependent forces that are caused by light near

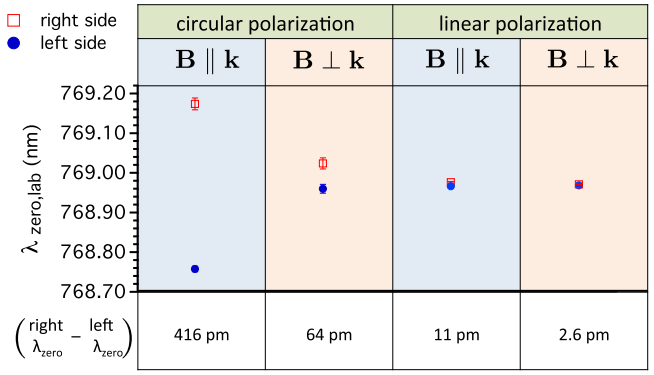

FIG. 6. λ_{zero} measurement as a function of optical polarization and magnetic field orientation. Data with circularly polarized laser light are from [22] and were taken with $v \approx 1600$ m/s atom beams. Data with linearly polarized light were take with $v \approx 2900$ m/s atom beams. Open red squares show measurements with the laser beam on the right side of the interferometer and solid blue circles show measurements on the left side.

a tune-out wavelength. In [22] we demonstrated that $\lambda_{\text{zero,lab}}$ is more sensitive to Ω_E when we use circularly polarized light, magnetic fields parallel to the light propagation (along $\hat{z}$), and atom beams with broad velocity distributions. For the λ_{zero} measurement reported here we reduced the sensitivity to Ω_E by using linearly polarized light, a transverse magnetic field (along $\hat{x}$), and a narrow atom beam velocity distribution. To create those conditions in the laboratory we installed a polarizer immediately prior to the MPC inside the vacuum system, we applied a 10-G transverse magnetic field with coils outside vacuum, and we used a 50-μm-diam nozzle for the supersonic beam jet to obtain an rms velocity spread of $\sigma_v = v_0/16$, where $v_0 = 2.9$ km/s is the most probable atomic velocity in the beam.

To monitor systematic errors due to Ω_E we measured how the root $\lambda_{\text{zero,lab}}$ depends on the sign of the irradiance gradient. Alternately illuminating the left and right sides of the atom interferometer reverses the sign of the atomic spin states (m_F numbers) that participate in phase echoes [22]. This changes the sign for the error ($\lambda_{\text{zero,lab}} - \lambda_{\text{zero}}$). Figure 6 summarizes how the difference $\lambda_{\text{zero,lab}}^{\text{right}} - \lambda_{\text{zero,lab}}^{\text{left}}$ was reduced by using linearly polarized light and the transverse magnetic field. We attribute the remaining difference to smaller but still nonzero spin-dependent forces that change with the irradiance gradient. Therefore, as suggested by Trubko *et al.* [22] we report the average $\frac{1}{2}(\lambda_{\text{zero,lab}}^{\text{right}} + \lambda_{\text{zero,lab}}^{\text{left}})$ for our measurement of λ_{zero}, as shown in Fig. 7. We estimate an additional systematic uncertainty of $(\lambda_{\text{zero,lab}}^{\text{right}} - \lambda_{\text{zero,lab}}^{\text{left}})/10 = 0.26$ pm associated with this averaging procedure. This uncertainty accounts for the fact that the magnitude and uniformity of the irradiance gradient, and hence the size of the systematic shift, can be slightly different when we reverse the sign of the irradiance gradient by moving the MPC from left to right.

VI. RESULTS

Here we summarize the data acquisition, analysis, and error budget. Data in Fig. 8 were acquired with light chopped on or off in between every file. Each file index (point) represents 5 s

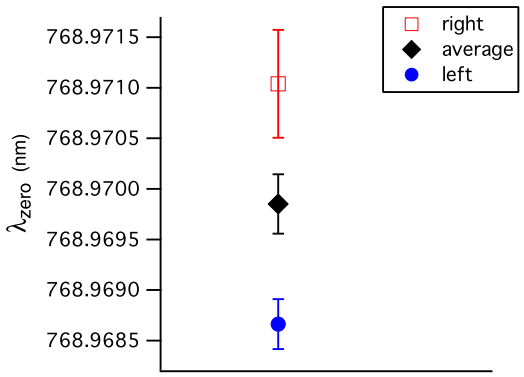

FIG. 7. Determination of λ_{zero} from the average $\frac{1}{2}(\lambda^{right}_{zero,lab} + \lambda^{left}_{zero,lab})$. Only statistical error bars of two times the standard error of the mean are shown. Systematic corrections total 0.3 pm, and systematic uncertainties totaling 0.3 pm are later added before a final result is presented for λ_{zero}.

of data. The wavelength of light was automatically switched every 125 s, and the laser wavelength was measured with a Bristol Instruments 621B wavemeter and recorded four times per second. Files with laser wavelength changes greater than 0.1 pm were ignored. The light-off data were used to remove the (∼6 rad/h) phase drift. Twenty minutes of data from a series of 220 files shown in Fig. 8(a) were used to

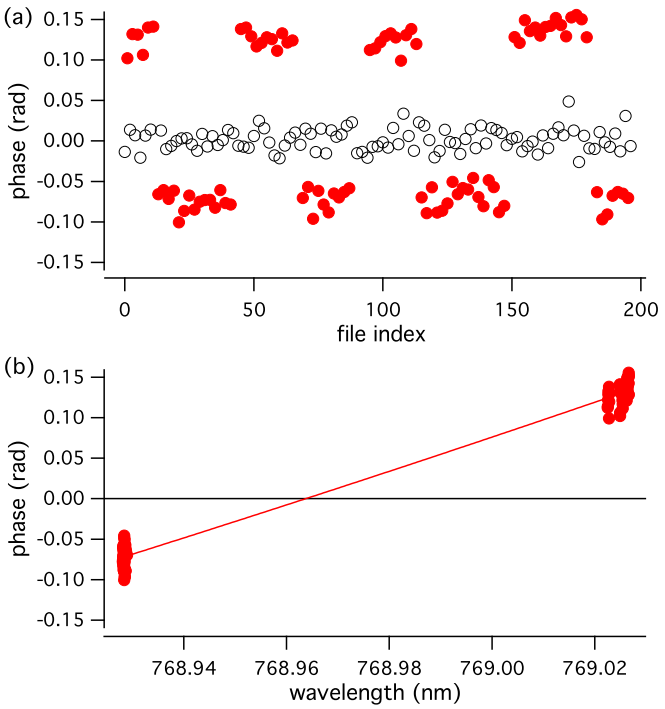

FIG. 8. (a) Phase data for the laser shining on the right path of the interferometer. Each file contains 5 s of data. Laser light from the tapered amplifier was chopped on or off in between every file. Light-on data are shown in solid red circles; light-off data are shown in open black circles. After 24 files the seed laser wavelength was automatically changed. (b) Phase data from (a) vs laser wavelength. Corrections for the net Doppler shift and broadband laser light have not been applied to the shown data in (a) and (b).

TABLE I. Error budget for the λ_{zero} measurement. Statistical and systematic uncertainties added in quadrature combine to make the total uncertainty of 0.4 pm. Corrections due to known systematic shifts are also shown. The left and/or right shift refers to the error from the difference in λ_{zero} measurements when the irradiance gradient is greater on either the left or right arms of the atom interferometer, as shown in Figs. 6 and 7. The left and/or right shift depends on the optical polarization, the magnetic field orientation, the Earth's rotation rate, and the atom beam velocity distribution, as described in this paper and in [22].

Source of error	Correction (pm)	Uncertainty (pm)
2× Standard error of the mean		0.29
Doppler shift	+0.21	0.10
Broadband light	+0.08	0.08
Left and/or right shift		0.26
Total	+0.29	0.41

make $\phi(\lambda)$ spectra shown in Fig. 8(b). We obtain a λ_{zero} measurement from this spectrum by finding the root of a $\phi(\lambda)$ fit. The fitting procedure uses χ-squared minimization and a theoretical spectrum given by Eq. (3), where $\phi(\omega)$ is simplified to $\phi(\omega) = b\alpha(\omega)$ and $\alpha(\omega)$ is shown in Eqs. (17) and (18). R and b are the free parameters. This analysis is further described in [2]. Ninety-one data sets similar to Fig. 8, some longer in duration than others, representing over 30 h of data in total, were compiled on a total of 9 different days to make 91 separate λ_{zero} measurements.

We compared results using the mean of all the data, the trimmed mean using the central 80% of the data, the weighted average using error bars that come from finding roots of individual $\phi(\lambda)$ data sets, and the trimmed weighted mean [27]. The results were all within 0.3 pm, and the statistical uncertainty (standard error of the mean) using these different methods ranged from 0.15 to 0.24 pm. For the final result we used the trimmed weighted means for $\lambda^{right}_{zero,lab}$ and $\lambda^{left}_{zero,lab}$ shown in Fig. 6.

The error budget for this λ_{zero} measurement is presented in Table I. The statistical uncertainty in λ_{zero} that we report, 0.3 pm, is twice the standard error of the mean [27]. Table I also summarizes the three types of systematic errors we discussed in the sections on decoherence spectroscopy, tuning out broadband light, and minimizing errors due to Ω_E. These errors in turn are related to Doppler shifts, broadband light, and optical polarization. Table I summarizes the correction (if any) and the uncertainty due to each source. Our final result with corrections applied and statistical and systematic uncertainties added in quadrature is $\lambda_{zero} = 768.9701(4)$ nm.

VII. DISCUSSION

Several calculations of tune-out wavelengths [7–14,16] use the sum-over-states approach to calculate the dynamic polarizability $\alpha(\omega)$, expressed in terms of reduced dipole matrix elements $\langle i \| D \| k \rangle$ or oscillator strengths f_{ik}. For K

between the $D1$ and $D2$ lines,

$$\alpha(\omega) = \frac{e^2 f_{D1}}{m\left(\omega_{D1}^2 - \omega^2\right)} + \frac{e^2 f_{D2}}{m\left(\omega_{D2}^2 - \omega^2\right)} + \alpha_{\rm r} = \frac{\omega_{D1}|\langle 4s_{1/2}\|D\|4p_{1/2}\rangle|^2}{3\hbar\left(\omega_{D1}^2 - \omega^2\right)} + \frac{\omega_{D2}|\langle 4s_{1/2}\|D\|4p_{3/2}\rangle|^2}{3\hbar\left(\omega_{D2}^2 - \omega^2\right)} + \alpha_{\rm r}, \quad (17)$$

where ω_{D1} and ω_{D2} are atomic resonance frequencies, and $\alpha_{\rm r} = \alpha_{\rm tail} + \alpha_{\rm core} + \alpha_{\rm vc}$ includes residual contributions from all transitions except the principle $D1$ and $D2$ transitions, contribution from core electrons, and the contribution from valence-core coupling [12,35–38]. Theoretical values for $\alpha_{\rm r}$ have been calculated by several theorists including [12,35,39]. Using our $\lambda_{\rm zero}$ measurement of 768.9701(4) nm and the theoretical $\alpha_{\rm r}(\lambda_{\rm zero}) = 6.7009$ a.u. [12], we report the ratio of $D1$ and $D2$ line strengths for K as

$$R = \frac{S_{D2}}{S_{D1}} = \frac{|\langle 4s\|D\|4p_{3/2}\rangle|^2}{|\langle 4s\|D\|4p_{1/2}\rangle|^2} = 1.9977(11) \quad (18)$$

and the ratio of oscillator strengths

$$\rho = \frac{f_{D2}}{f_{D1}} = R\left(\frac{\omega_{D2}}{\omega_{D1}}\right) = 2.0066(11) \quad (19)$$

and the ratios of lifetimes

$$\frac{\tau_{4p_{1/2}}}{\tau_{4p_{3/2}}} = \frac{R}{2}\left(\frac{\omega_{D2}}{\omega_{D1}}\right)^3 = 1.01223(55). \quad (20)$$

Independent measurements of state lifetimes by Volz *et al.* [40] established the value $R = 1.9989(74)$. Holmgren *et al.* [2] found $R = 2.0005(40)$ based on a tune-out-wavelength measurement. Now, with a more precise $\lambda_{\rm zero}$ measurement we report $R = 1.9977(11)$. This result has 6.7 times smaller uncertainty for R than was experimentally measured without tune-out wavelengths. The uncertainty of 0.0011 for R reported here primarily comes from uncertainty in the measured $\lambda_{\rm zero}$. For comparison, a contribution of 0.0001 to the uncertainty in R is due to a 5% uncertainty in $\alpha_{\rm core}$. Our experiments with a multipass cavity have improved the statistical precision in the $\lambda_{\rm zero}$ measurement by a factor of 6 compared to [2]. However, due to the systematic shifts that we have described, the experiment with a multipass cavity has only improved the total uncertainty for R by a factor of 3.6 as compared to [2].

If we combine this measurement of $\lambda_{\rm zero}$ with our recent measurement of static polarizability for potassium of

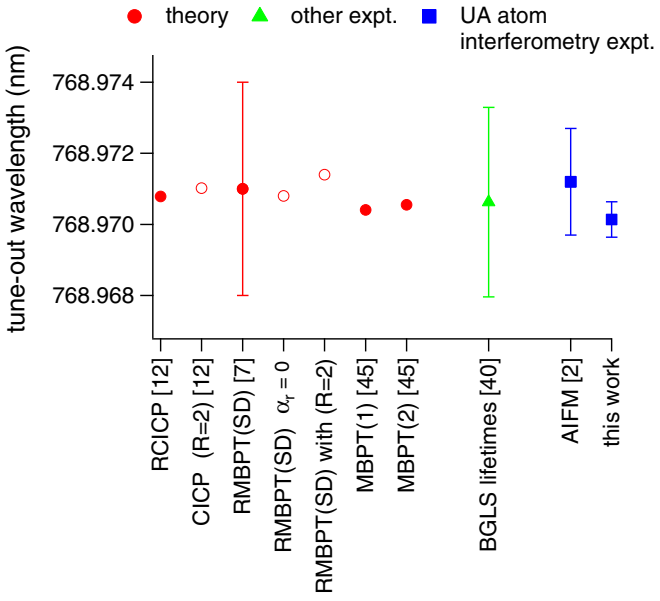

FIG. 9. Comparison of measured and calculated values for the longest $\lambda_{\rm zero}$ for potassium. Calculations are shown in solid red circles. Calculations that assume $R = 2$ or $\alpha_{\rm r} = 0$ are shown with open red circles. The result from lifetime measurements is shown with solid green triangles. Measurements made with atom interferometry are shown with solid blue squares.

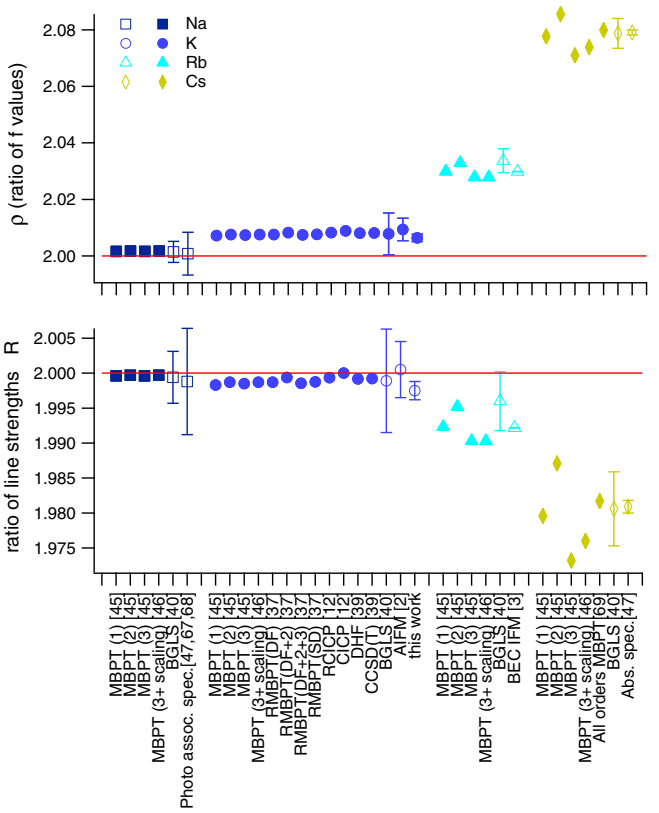

FIG. 10. Theoretical calculations shown with solid circles, and experimental measurements shown with open circles, of ρ, the ratio of oscillator strengths (top), and R, the ratio of line strengths (bottom): MBPT refers to many-body perturbation theory and the number in parentheses refers to the order [45]. RMBPT refers to relativistic MBPT [37]. DF refers to Dirac-Fock basis orbitals [37]. SD refers to the single-double all order method [37]. RCICP refers to the relativistic configuration interaction plus core polarization approach [12]. CICP refers to the configuration interaction plus core polarization method [12]. DHF refers to the Dirac-Hartree-Fock method [39]. CCSD refers to the singles-doubles coupled-cluster method [39]. BGLS refers to beam-gas-laser spectroscopy measurements [40]. AIFM refers to atom interferometry measurements. BEC IFM refers to interferometry measurements made with Bose-Einstein condensates [3]. Photo assoc. spec. refers to photoassociation spectroscopy [47,67,68]. Abs. spec. refers to absorption spectroscopy [47].

$\alpha(0) = 289.7(3)$ a.u. [41,42] and the theoretical value $\alpha_r(0) = 6.26(33)$ a.u. [35], then we can report the values for individual oscillator strengths, dipole matrix elements, lifetimes, and line strengths with reduced uncertainty. All of these physical quantities are related as described in [42]. For lifetimes of the $4p_{1/2}$ and $4p_{3/2}$ states, we report $\tau_{4p_{1/2}} = 26.78(4)$ ns and $\tau_{4p_{3/2}} = 26.46(4)$ ns. As a comparison, Volz *et al.* report independent lifetime measurements $\tau_{4p_{1/2}} = 26.79(7)$ ns and $\tau_{4p_{3/2}} = 26.45(7)$ ns [40]. These results are consistent, but ours offer a smaller uncertainty. Other experiments by Wang *et al.* and Falke *et al.* are sensitive to the average of lifetimes, but not the difference (or ratio) of the $\tau_{4p_{1/2}}$ and $\tau_{4p_{1/2}}$ lifetimes [43,44].

Figure 9 compares calculations and measurements for the longest tune-out wavelength for potassium. We show experimental results in Fig. 9 from this work, from Holmgren *et al.* [2], and the λ_{zero} inferred from the independent measurements of the $4p_{3/2}$ and $4p_{1/2}$ state lifetimes by Volz *et al.* [40]. The only calculation with a published uncertainty so far is by Arora *et al.* [7], who presented $\lambda_{zero} = 768.971$ nm with a 3-pm uncertainty based on many-body perturbation theory (MBPT) calculations. Relativistic configuration interaction with core polarization (RCICP) calculations by Jiang *et al.* [12] showed $\lambda_{zero} = 768.97077$ nm. We also used results for dipole matrix elements from Johnson *et al.* [45,46], which were already discussed in the context of R by [47], in order to infer λ_{zero} using Eq. (17).

Along with the theoretical results [7,9,45,46] we plot-shifted λ_{zero} values that show how the value of λ_{zero} from Aurora *et al.* would change if we assume a value of zero for α_r in Eq. (17). Setting $\alpha_r = 0$ decreases λ_{zero} by only 0.2 pm [12]. Then we show a shifted prediction for λ_{zero} that we produced using Eq. (17) and the hypothesis that $R = 2$ (but still using the measured values for λ_{D1} and λ_{D2}). Setting $R = 2$ increases λ_{zero} by 0.4 pm.

Historical discussions of the oscillator strength ratio anomaly problem [37,48–60] explain why R and ρ deviate from the statistical value of 2 that would be naïvely expected from the statistical degeneracies of the $4p_{3/2}$ and $4p_{1/2}$ states. Both relativistic effects and core polarization effects are important, as pointed out by Fermi in 1930 [61] and discussed extensively by Migdalek [48–50,62–66]. Figure 10 shows theoretical predictions and experimental measurements for R and ρ for Na, K, Rb, and Cs. This shows that $R < 2$ and $\rho > 2$ are trends that get more pronounced for heavier atoms. With the λ_{zero} measurement presented in this work, we have shown that $R < 2$ with 2σ significance and $\rho > 2$ with 5σ significance for K atoms, where σ here refers to the total uncertainty in our λ_{zero} measurement summarized in Table I. The λ_{zero} measurement presented here constitutes a significant demonstration of the oscillator strength ratio anomaly for potassium.

To conclude, λ_{zero} measurements have stimulated creative experimental work in several laboratories, such as synchronized pulsing of light on atoms in a time-orbiting potential trap so as to control $\vec{k} \cdot \vec{B}$ [3], coherent addition of diffraction amplitudes from multiple short light pulses [1], and novel studies of atom trap dynamics [4]. In the work presented here, we developed a multipass cavity interaction region for an atom interferometer. We developed decoherence spectroscopy. We also used the concept of a broadband tune-out wavelength. These methods help to improve λ_{zero} measurements and demonstrate techniques for atom interferometry.

ACKNOWLEDGMENTS

We thank Jaggar D. Henzerling and Matthew J. Lichtenberger for discussing systematic error analysis. This work is supported by NSF Grant No. 1306308 and a NIST PMG. R.T. and M.D.G. thank NSF GRFP Grant No. DGE-1143953 for support.

[1] C. D. Herold, V. D. Vaidya, X. Li, S. L. Rolston, J. V. Porto, and M. S. Safronova, Precision Measurement of Transition Matrix Elements via Light Shift Cancellation, Phys. Rev. Lett. **109**, 243003 (2012).

[2] W. F. Holmgren, R. Trubko, I. Hromada, and A. D. Cronin, Measurement of a Wavelength of Light for Which the Energy Shift for an Atom Vanishes, Phys. Rev. Lett. **109**, 243004 (2012).

[3] R. H. Leonard, A. J. Fallon, C. A. Sackett, and M. S. Safronova, High-precision measurements of the ^{87}RB D-line tune-out wavelength, Phys. Rev. A **92**, 052501 (2015).

[4] B. M. Henson, R. I. Khakimov, R. G. Dall, K. G. H. Baldwin, Li-Yan Tang, and A. G. Truscott, Precision Measurement for Metastable Helium Atoms of the 413 nm Tune-Out Wavelength at Which the Atomic Polarizability Vanishes, Phys. Rev. Lett. **115**, 043004 (2015).

[5] F. Schmidt, D. Mayer, M. Hohmann, T. Lausch, F. Kindermann, and A. Widera, Precision measurement of the ^{87}RB tune-out wavelength in the hyperfine ground state $F = 1$ at 790 nm, Phys. Rev. A **93**, 022507 (2016).

[6] M. S. Safronova, C. J. Williams, and C. W. Clark, Relativistic many-body calculations of electric-dipole matrix elements, lifetimes, and polarizabilities in rubidium, Phys. Rev. A **69**, 022509 (2004).

[7] B. Arora, M. S. Safronova, and C. W. Clark, Tune-out wavelengths of alkali-metal atoms and their applications, Phys. Rev. A **84**, 043401 (2011).

[8] T. Topcu and A. Derevianko, Tune-out wavelengths and landscape-modulated polarizabilities of alkali-metal Rydberg atoms in infrared optical lattices, Phys. Rev. A **88**, 053406 (2013).

[9] J. Mitroy and Li-Yan Tang, Tune-out wavelengths for metastable helium, Phys. Rev. A **88**, 052515 (2013).

[10] F. Le Kien, P. Schneeweiss, and A. Rauschenbeutel, Dynamical polarizability of atoms in arbitrary light fields: General theory and application to cesium, Eur. Phys. J. D **67**, 1 (2013).

[11] J. Jiang and J. Mitroy, Hyperfine effects on potassium tune-out wavelengths and polarizabilities, Phys. Rev. A **88**, 032505 (2013).

[12] J. Jiang, L.-Y. Tang, and J. Mitroy, Tune-out wavelengths for potassium, Phys. Rev. A **87**, 032518 (2013).

[13] Y. Cheng, J. Jiang, and J. Mitroy, Tune-out wavelengths for the alkaline-earth-metal atoms, Phys. Rev. A **88**, 022511 (2013).

[14] M. S. Safronova, Z. Zuhrianda, U. I. Safronova, and C. W. Clark, Extracting transition rates from zero-polarizability spectroscopy, Phys. Rev. A **92**, 040501 (2015).

[15] W.-W. Yu, R.-M. Yu, and Y.-J. Cheng, Tune-out wavelengths for the Rb atom, Chin. Phys. Lett. **32**, 123102 (2015).

[16] L. J. LeBlanc and J. H. Thywissen, Species-specific optical lattices, Phys. Rev. A **75**, 053612 (2007).

[17] J. Catani, G. Barontini, G. Lamporesi, F. Rabatti, G. Thalhammer, F. Minardi, S. Stringari, and M. Inguscio, Entropy Exchange in a Mixture of Ultracold Atoms, Phys. Rev. Lett. **103**, 140401 (2009).

[18] J. Catani, L. De Sarlo, G. Barontini, F. Minardi, and M. Inguscio, Degenerate Bose-Bose mixture in a three-dimensional optical lattice, Phys. Rev. A **77**, 011603 (2008).

[19] A. J. Daley, M. M. Boyd, J. Ye, and P. Zoller, Quantum Computing with Alkaline-Earth-Metal Atoms, Phys. Rev. Lett. **101**, 170504 (2008).

[20] B. Gadway, D. Pertot, J. Reeves, and D. Schneble, Probing an ultracold-atom crystal with matter waves, Nat. Phys. **8**, 544 (2012).

[21] A. Steffen, A. Alberti, W. Alt, N. Belmechri, S. Hild, M. Karski, A. Widera, and D. Meschede, Digital atom interferometer with single particle control on a discretized space-time geometry, Proc. Natl. Acad. Sci. USA **109**, 9770 (2012).

[22] R. Trubko, J. Greenberg, M. T. St. Germaine, M. D. Gregoire, W. F. Holmgren, I. Hromada, and A. D. Cronin, Atom Interferometer Gyroscope with Spin-Dependent Phase Shifts Induced by Light near a Tune-Out Wavelength, Phys. Rev. Lett. **114**, 140404 (2015).

[23] R. Chamakhi, H. Ahlers, M. Telmini, C. Schubert, E. M. Rasel, and N. Gaaloul, Species-selective lattice launch for precision atom interferometry, New J. Phys. **17**, 123002 (2015).

[24] David W. Keith, Christopher R. Ekstrom, Quentin A. Turchette, and David E. Pritchard, An Interferometer for Atoms, Phys. Rev. Lett. **66**, 2693 (1991).

[25] P. R. Berman, *Atom Interferometry* (Academic Press, San Diego, 1997).

[26] A. D. Cronin, J. Schmiedmayer, and D. E. Pritchard, Optics and interferometry with atoms and molecules, Rev. Mod. Phys. **81**, 1051 (2009).

[27] P. R. Bevington and D. Keith Robinson, *Data Reduction and Error Analysis* (McGraw-Hill, New York, 2003).

[28] P. Hamilton, M. Jaffe, J. M. Brown, L. Maisenbacher, B. Estey, and H. Müller, Atom Interferometry in an Optical Cavity, Phys. Rev. Lett. **114**, 100405 (2015).

[29] R. Trubko and A. D. Cronin, Decoherence spectroscopy for atom interferometry, Atoms **4**, 25 (2016).

[30] V. Bolpasi and W. von Klitzing, Double-pass tapered amplifier diode laser with an output power of 1 W for an injection power of only 200 μW, Rev. Sci. Instrum. **81**, 113108 (2010).

[31] Eagleyard EYP-TPA-0765-02000.

[32] Eagleyard EYP-RWE-0790-04000.

[33] Thorlabs SM-600.

[34] Photon Control model SPM-002-C.

[35] M. S. Safronova, B. Arora, and C. W. Clark, Frequency-dependent polarizabilities of alkali-metal atoms from ultraviolet through infrared spectral regions, Phys. Rev. A **73**, 022505 (2006).

[36] M. S. Safronova, U. I. Safronova, and C. W. Clark, Magic wavelengths for optical cooling and trapping of potassium, Phys. Rev. A **87**, 052504 (2013).

[37] U. I. Safronova and M. S. Safronova, High-accuracy calculation of energies, lifetimes, hyperfine constants, multipole polarizabilities, and blackbody radiation shift in ^{39}K, Phys. Rev. A **78**, 052504 (2008).

[38] W. R. Johnson, D. Kolb, and K.-N. Huang, Electric-dipole, quadrupole, and magnetic-dipole susceptibilities and shielding factors for closed-shell ions of the He, Ne, Ar, Ni (Cu+), Kr, Pb, and Xe isoelectronic sequences, At. Data Nucl. Data Tables **28**, 333 (1983).

[39] D. K. Nandy, Yashpal Singh, B. P. Shah, and B. K. Sahoo, Transition properties of a potassium atom, Phys. Rev. A **86**, 052517 (2012).

[40] U. Volz and H. Schmoranzer, Precision lifetime measurements on alkali atoms and on helium by beam-gas-laser spectroscopy, Phys. Scr. **1996**, 48 (1996).

[41] M. D. Gregoire, I. Hromada, W. F. Holmgren, R. Trubko, and A. D. Cronin, Measurements of the ground-state polarizabilities of Cs, Rb, and K using atom interferometry, Phys. Rev. A **92**, 052513 (2015).

[42] M. D. Gregoire, N. Brooks, R. Trubko, and A. D. Cronin, Analysis of polarizability measurements made with atom interferometry, Atoms **4**, 21 (2016).

[43] H. Wang, J. Li, X. T. Wang, C. J. Williams, P. L. Gould, and W. C. Stwalley, Precise determination of the dipole matrix element and radiative lifetime of the K 39 4p state by photoassociative spectroscopy, Phys. Rev. A **55**, R1569 (1997).

[44] St. Falke, I. Sherstov, E. Tiemann, and Ch. Lisdat, The $A\,^1\Sigma_u^+$ state of K_2 up to the dissociation limit, J. Chem. Phys. **125**, 224303 (2006).

[45] W. R. Johnson, M. Idrees, and J. Sapirstein, Second-order energies and third-order matrix elements of alkali-metal atoms, Phys. Rev. A **35**, 3218 (1987).

[46] W. R. Johnson, Z. W. Liu, and J. Sapirstein, Transition rates for lithium-like ions, sodium-like ions, and neutral alkali-metal atoms, At. Data Nucl. Data Tables **64**, 279 (1996).

[47] R. Rafac and C. Tanner, Measurement of the ratio of the cesium D-line transition strengths, Phys. Rev. A **58**, 1087 (1998).

[48] J. MigdaŁek and Y.-K. Kim, Core polarization and oscillator strength ratio anomaly in potassium, rubidium and caesium, J. Phys. B: At. Mol. Opt. Phys. **31**, 1947 (1998).

[49] J. MigdaŁek and E. Banasińska, Implicit and explicit treatment of valence-core electron exchange and core polarization in model potentials, J. Quant. Spectrosc. Radiat. Transfer **39**, 409 (1988).

[50] J. Migdalek and W. E. Baylis, Local approximations for the exchange interaction between valence and core electrons, Phys. Rev. A **22**, 22 (1980).

[51] A. Corney and K. Gardner, A new method for determining f-values using stimulated electronic raman scattering in atomic vapours, J. Phys. D: Appl. Phys. **11**, 1815 (1978).

[52] W. Hansen, The application of polarisation-influenced Thomas-Fermi ion models to alkali-atom transitions, J. Phys. B: At. Mol. Phys. **17**, 4833 (1984).

[53] C.-M. Huang and C. C. Wang, Oscillator Strength for Principal Series Transitions to the High Rydberg States of Potassium, Phys. Rev. Lett. **46**, 1195 (1981).

[54] M. Szulkin and J. Karwowski, Core polarisation and relativistic effects in the alkali atoms, J. Phys. B: At. Mol. Phys. **14**, 4729 (1981).

[55] G. H. Jeung, J. P. Malrieu, and J. P. Daudey, Inclusion of core-valence correlation effects in pseudopotential calculations. I. Alkali atoms and diatoms, J. Chem. Phys. **77**, 3571 (1982).

[56] I. Martin and C. Barrientos, Core-polarization effects in the alkali atoms: Oscillator-strength calculations, Can. J. Phys. **64**, 867 (1986).

[57] I. Martin, C. Lavín, and C. Barrientos, Systematic trends along the potassium sequence: Study of $ns\,^2S$–$mp\,^2P^0$ transitions, Can. J. Phys. **69**, 1273 (1991).

[58] C. Barrientos and I. Martin, Core-polarization effects in subordinate series of the alkali atoms, Can. J. Phys. **67**, 996 (1989).

[59] P. M. Stone and K. Yong-Ki, Electron-impact cross sections for ground state to np excitations of sodium and potassium, J. Res. Natl. Inst. Stand. Technol. **109**, 505 (2004).

[60] J. Karwowski and M. Szulkin, Relativistic calculations on the alkali atoms by a modified Hartree-Fock method, J. Phys. B: At. Mol. Phys. **14**, 1915 (1981).

[61] E. Fermi, Über das intensitätsverhältnis der dublettkomponenten der alkalien, Z. Phys. **59**, 680 (1930).

[62] J. Migdałek, Model potential approach to core polarisation in SCF calculations, Phys. Scr. **2002**, 47 (2002).

[63] J. Migdalek and M. Garmulewicz, The relativistic ab initio model potential versus Dirac-Fock oscillator strengths for silver and gold isoelectronic sequences, J. Phys. B: At. Mol. Opt. Phys. **33**, 1735 (2000).

[64] J. Migdalek and M. Wyrozumska, Relativistic oscillator strengths for the Cs isoelectronic sequence and collapse of F and D orbitals, J. Quant. Spectrosc. Radiat. Transfer **37**, 581 (1987).

[65] J. Migdałek and W. E. Baylis, Relativistic Hartree-Fock and model-potential ionization energies and oscillator strengths for transitions in the principal, sharp, and diffuse series of neutral rubidium and silver with allowance for core polarization, Can. J. Phys. **57**, 1708 (1979).

[66] J. Migdalek and W. E. Baylis, Influence of atomic core polarisation on oscillator strengths for $^2S_{1/2}$-$^2P_{1/2,3/2}$ and $^2P_{1/2,3/2}$-$^2D_{3/2,5/2}$ transitions in Cu I, Ag I and Au I spectra, J. Phys. B: At. Mol. Opt. Phys. **11**, L497 (1978).

[67] E. Tiemann, H. Knöckel, and H. Richling, Long-range interaction at the asymptote 3s+3 of Na_2, Z. Phys. D **37**, 323 (1996).

[68] K. M. Jones, P. S. Julienne, P. D. Lett, W. D. Phillips, E. Tiesinga, and C. J. Williams, Measurement of the atomic Na($3p$) lifetime and of retardation in the interaction between two atoms bound in a molecule, Europhys. Lett. **35**, 85 (1996).

[69] S. A. Blundell, J. Sapirstein, and W. R. Johnson, High-accuracy calculation of parity nonconservation in cesium and implications for particle physics, Phys. Rev. D **45**, 1602 (1992).